Computational Flow Models in Cerebral Congenital Aneurisms

Marc Thiriet

INSTITUT NATIONAL DE RECHERCHE EN INFORMATIQUE ET EN AUTOMATIQUE

Computational Flow Models in Cerebral Congenital Aneurisms

M. Thiriet

N° 3768
Septembre 1999

THÈME 4

INRIA
ROCQUENCOURT

Computational Flow Models in Cerebral Congenital Aneurisms

Thiriet M.*

Thème 4 — Simulation et optimisation
de systèmes complexes
Projet M3N

Rapport de recherche n ° 3768 — Septembre 1999 — 38 pages

Abstract: Congenital cerebral aneurisms occur at the bifurcations of cerebral arteries. Two kinds of models of rigid aneurisms are investigated: a basilar-like bifurcation and a ophtalmica-carotis-like bifurcation aneurisms. Because the geometry of the aneurism neck and of the transition zone, which both affect the local flow, was not accurately known, two-dimensional models are developed. The largest cerebral arteries are explored using MR velocimetry to determine boundary conditions and flow repartition at branch points. The numerical solution of the Navier-Stokes equations for incompressible flows is obtained using the finite element method. The three main flow characteristics are: (i) swirls in the aneurism and in the transition zone, associated to slow flow at the aneurism dome, (ii) flow separation in the branches, and (iii) high pressure zones, more or less large, in the cavity or in the neck. High pressure zones responsible of aneurism rupture have also been observed in coil-obliterated cavity models. Similar results are observed in three-dimensional models.

Key-words: Cerebral Aneurisms, Finite Element, Navier-Stokes Equations

(Résumé : tsvp)

* Email: Marc.Thiriet@inria.fr

Unité de recherche INRIA Rocquencourt
Domaine de Voluceau, Rocquencourt, BP 105, 78153 LE CHESNAY Cedex (France)
Téléphone : 01 39 63 55 11 - International : +33 1 39 63 55 11
Télécopie : (33) 01 39 63 53 30 - International : +33 1 39 63 53 30

Modèles numériques de l'écoulement dans des anévrismes cérébraux congénitaux.

Résumé : Les anévrismes cérébraux congénitaux se développent dans les embranchements des artères cérébrales de gros et moyen calibre. Deux types de modèles d'anévrismes rigides sont explorés : un anévrisme développé à l'apex d'une bifurcation symétrique, munie d'une zone de transition anatomique, du type anévrisme de la division du tronc basilaire et un anévrisme siègeant dans un embranchement d'un tronc courbe qui donne naissance à une branche de calibre plus faible, du type anévrisme carotido-ophtalmique. La cavité anévrismale est soit libre, soit obstruée partiellement ou complètement, de manière à simuler l'anévrisme traité par voie endovasculaire. Il s'agit, dans ce dernier cas, de rechercher d'éventuelles possibilités de recanalisation postthérapeutiques de la lésion. Les équations de conservation de la masse et de la quantité de mouvement sont résolues par la méthode des éléments finis dans le cas du fluide newtonien incompressible. Les trois caractéristiques de l'écoulement sont : la présence de tourbillons dans la cavité anévrismale, au niveau du collet et de la zone de transition, l'apparition de décollements dans les branches et l'existence de zones à très forte pression, soit dans l'anévrisme, soit au niveau du collet. Le champ de pression permet d'expliquer l'expansion de l'anévrisme et sa rupture, soit au niveau du dôme, soit au niveau du collet, ainsi que les échecs de la thérapie endovasculaire.

Mots-clé : Anévrismes cérébraux sacculaires congénitaux, Champ de pression, Eléments finis, Equations de Navier-Stokes.

1 Introduction

The problem formulation is based on two questions: (i) why the aneurism rupture risk depends on the aneurism type ? and (ii) why a post-therapeutic development of the aneurism may occur ? Blood flow is investigated in cerebral aneurisms because of the stress-dependent genesis and evolution of these wall expansions, although the relationship between the hemodynamic stresses and the arterial wall remodeling is not clearly understood. The danger of increased pressure and sudden rise and fall in pulse rate have been pointed out in lumped parameter models of intracranial aneurisms [1],[2]. The higher the intra-aneurismal pressure, the greater the probability of aneurism rupture [3].

Two main classes of aneurisms may be defined according to the configuration: (i) the saccular lesion and (ii) the fusiform dilatation, which develops usually on diseased artery walls. Numerical and experimental steady flow investigations have been recently carried out on axisymmetric models of straight segments with spindle-shaped aneurisms for a given range of Reynolds number Re (computed from the cross-sectional average velocity and the diameter of the uniform entrance segment), either $[500 - 2600]$ [4] or $[300 - 3600]$ [5].

Two kinds of saccular aneurisms are observed whether they are observed on a curved section of the artery, or at a branching segment of the arterial network. The first type is defined as lateral aneurism, which may be either postinfectious or posttraumatic, the origin being, often, not well understood (Fig. 1 and 2). However, posthaemorrhagic aneurisms are caused by the bleeding of the wall vasa vasora.

The frequency of saccular aneurisms in the population may be estimated to be about 1 %. However, it can increase up to 10 % in members of patient families. Hemorrhage induced by intracranial aneurism rupture and stroke (due to emboli, vasospasm or external compression of the blood vessels) are associated with high mortality. The rupture can occur either at the neck ($\sim$ 10 %) or at the pouch, either in the edges ($\sim$ 30 %) or in the fundus ($\sim$ 60 %).

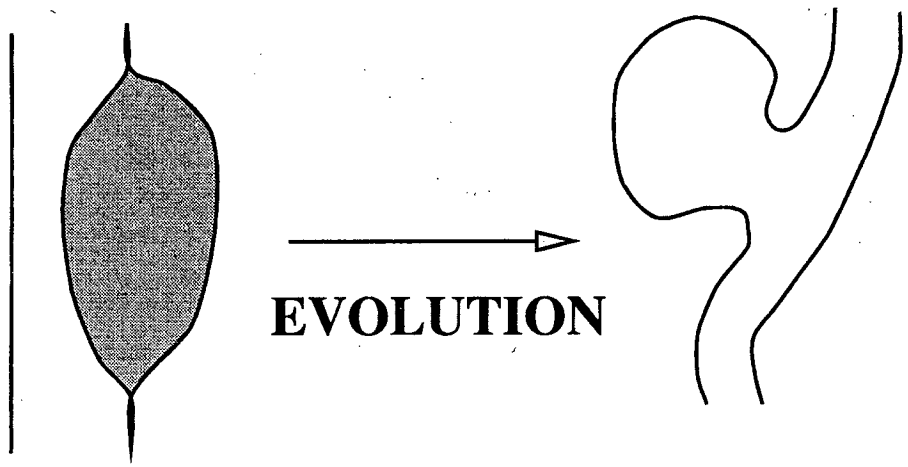

Figure 1: Clinical observation 1: aneurism in a curved segment of the intrenal carotid artery upstream from the carotid bifurcation following a within-wall haemorrhage. A resultant vessel stenosis developed and later on an aneurism appears.

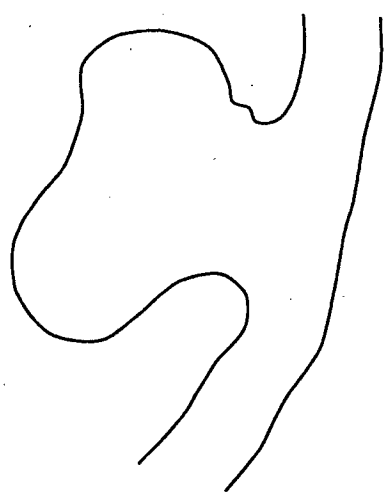

Figure 2: Clinical observation 2: aneurism in the curved segment V2 of the vertebral artery (C3 segment), following either a traumatism or an infection.

Cerebral aneurisms are classified into three categories according to the largest width w of the aneurism sac (see Fig. 3 for the geometry nomenclature): (i) small (w < 12 mm), (ii) large (12 ≤w ≤ 25 mm) and (iii) giant (w > 25 mm). They can also be divided into two groups according to the neck size, with a threshold of 4 mm between the small and wide necks (*e.g.* [6]). Other geometrical characteristics are given by the (i) pouch shape (round, oval; uni or multilobulated), (ii) the cerebral artery site and the angle between the greatest aneurismal length and the main-flow local direction, and (iii) the surroundings (subarachnoid space or cerebral tissues). The aneurism configuration affects the ratio between the volume flow rate Q_a which enters in the aneurism and the volume flow rate Q_d which moves directly in the downstream vessel segment. In giant aneurisms, Q_a/Q_d may be great.

Experimental and numerical models of lateral aneurisms arising from a straight vessel at a 90 degree angle have been investigated. The flow enters the aneurism via the downstream lip and reaches the sac central region. The fluid flows then back to the diseased vessel along the aneurismal walls, from the sac center or from the fundus. These fluid paths have been shown by laser-Doppler velocimetry through rigid and compliant models conveying steady ($400 \leq Re \leq 600$) and non-zero mean sinusoidal flow of Newtonian and non-Newtonian fluid [7]. Similar results are obtained in three-dimensional numerical simulations of pulsatile flow, with a superimposed sinusoidal component (mean Reynolds number, computed from the time mean cross-sectional average velocity, $\overline{\mathrm{Re}} \sim 130$, Stokes number $St = 2.5$) [8] or a physiological one ($\overline{\mathrm{Re}} = 200$, $St, \sim 7$) [9]. The curved pipe model is more appropriate because the characteristic bend nature of blood flow is taken into account. However, similar fluid circulation within the aneurismal cavity is found whatever the exploration method, flow visualisation and laser-Doppler velocimetry of steady ($Re = 150, 220$, Dean number $De = 57, 83$) and non-zero mean sinusoidal flow ($\overline{\mathrm{Re}} = 336$, $De = 128$, $St = 2.5$) in an aneurism model either at the outer bend or at the inner wall of a 180 degree bend [10], finite element approximation of the unsteady non-Newtonian flow field in an aneurism rigid model at the outer bend of a 90 degree bend [9], and angiography associated to Doppler sonography of constructed aneurisms in canine carotid artery [11]. Angiographic and ultra-sound Doppler examinations have shown

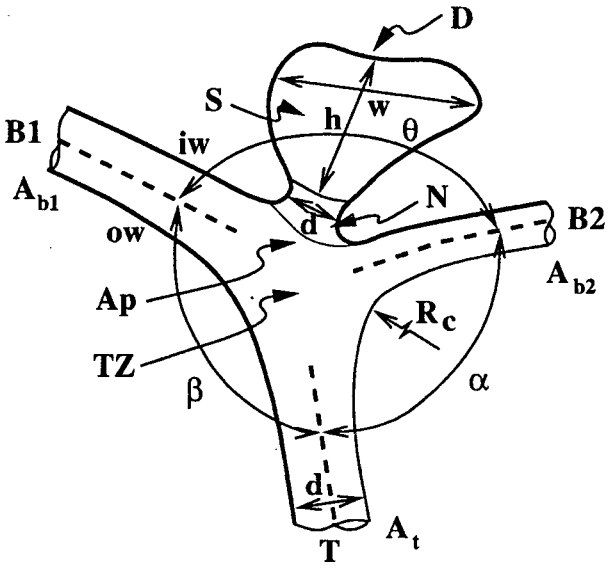

Figure 3: Schematic drawing of a saccular aneurism, with a right loculus, at the apex Ap of the bifurcation (area ratio: $\sum A_b/A_t$) of the intracranial artery network, with the name of the geometrical components. T: trunk (stem), with its displayed axis (dashed line), of cross-sectional area A_t, B: branch, of cross-sectional area A_b, TZ: transition zone, ow: outer bifurcation wall (but inner curvature wall), iw: inner wall, α, β, θ: branching angles (in terminal aneurisms, θ is the bifurcation angle, α and β are the lateral angles), R_c: local curvature radius ($d/2R_c$: curvature ratio), S: aneurismal sac (cavity, pouch) of width w and height h, N: aneurismal neck of diameter d, D: aneurismal dome (fundus).

that the flow features in lateral and in branch aneurisms are different [12].

The saccular aneurisms located at branching segments are subdivided into two groups: the branch and terminal aneurisms, whether the branching site provides a lateral branch or terminal branches respectively. Silicone transparent models, obtained from castings of cerebral arteries (*e.g.* [13]), are used to explore the flow as well as to calibrate medical imaging devices. However, a huge variability in aneurism geometry, which is very complex, exists. Consequently, the arterial lesion must be modelled, a strategy associated to the economy principle in data collection and processing, rather than to describe the arterial lesion set as completely as possible, without control of the physical factors. Experimental rigid and deformable models (*e.g.* [14][15]) are very useful to validate the numerical simulations, which give the full flow field and can much more easily provides the effects of various factors, with others variables being kept constant. A two-dimensional model of a pulsatile ($\overline{\mathrm{Re}} = 150$, where Re is the stem Reynolds number, $St = 1.5$) Newtonian and non-Newtonian flow in a symmetrical bifurcation (bifurcation angle of 80 degrees, area ratio, which is the sum of the cross-sectional areas of the daughter tubes to the cross-sectional area of the parent tube, of 1.2), with the wall lesion on the apex and the inner wall of a single branch has been carried out [16].

The present work is focused on the congenital saccular aneurisms of the cerebral artery network. Congenital saccular aneurisms may be observed at the bifurcations of cerebral arteries mainly the vessels afferent to and efferent from the Willis circle. The Willis circle is the main source of oxygenated blood supplied to the brain (Fig. 4). It conveys the blood from the carotis interna and the basilaris, formed by the junction of the left and right vertebralis. The basilar artery divides usually into two branches, the posterior cerebral arteries, while the internal carotid artery, after giving birth to the ophtalmic artery, divides into the middle and the anterior cerebral arteries. The Willis circle is composed from behind forwards by the basilar bifurcation and the posterior cerebrals, in anastomosis with the two internal carotids via the two posterior communicating arteries, the internal carotids and the two anterior cerebrals with the anterior communicating. Besides, the circle of Willis is, most often, only partially designed, one or two posterior communicatings being often

absent. Moreover, the internal carotid may give birth to the posterior cerebral.

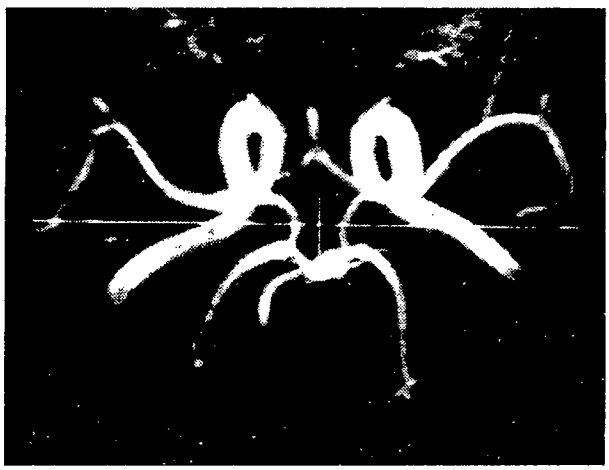

Figure 4: MR angiography of the cerebral arteries in the region of the Willis circle in a healthy female volunteer.

The arterial wall is made of three layers: (i) the intima with its wetted part, the endothelium, (ii) the media, predominantly composed of smooth muscle cells, and (iii) the external adventitia. The congenital saccular aneurism might develop in the region where the media is discontinuous due to the wall division into branch walls in association with deterioration in wall elasticae, which mark the boundary of the media with the adjoining wall tunicae.

Intravascular treatment consists in filling the aneurism cavity with coils (Fig. 5). The geometrical features, especially the sac and orifice sizes, are important short-term prognosis factors, because they affect the occlusion quality. The smaller the aneurism size, the better the cavity obliteration, for a given aneurism shape and location. The aneurism cavity is, very often, partially filled because the complete filling is very difficult to obtain: peroperative rupture must be avoided as well as arterial lumen obstruction with its thromboembolic risk. Furthermore, the coils are compressed by the blood flux and the thrombi on the coils retract. The coils can much less easily migrate when the aneurism

ostium is small. The probability of rupture of a treated aneurism becomes high when about one third of the cavity or more remains free. Besides, giant aneurisms can compress the downstream vessel segment. In such cases, coil treatment must be associated with a stent setting.

Figure 5: Aneurism of the basilar trunk bifurcation, before (left) and after (right, subtraction image) coil occlusion.

Numerical simulations are used in biomechanics to get the field of the mechanical quantities of interest and to test the effects of influence factors which can be varied while holding all other parameters constant. The finite element method, which ensures a within- and between-element continuity, is usually used because (i) it is a pertinent technique for complex configurations and (ii) it solves the fluid mechanics equations for various types of boundary conditions. The present work is aimed at studying bifurcation aneurisms, of arbitrary geometry, which mimic real lesions, before and after intravascular treatment with different occlusion volumes, in order to investigate the local flow behaviour and to assess posttherapeutic development of the lesion (Fig. 6). The fluid domain is composed of a trunk (inward flow), a transition zone, the branches (outward flows) and the saccular terminal or branch aneurism.

The pressure, which is responsible within the aneurismal wall for both an azimuthal distension and a radial compression, is assumed to play a major role on the development and the rupture of the aneurism, both phenomena being much less dependent on the shear stress. The rupture risk is indeed known to rise with increasing aneurism size and decreasing aneurism wall thickness. In particular, the pressure is very great on the impinged surface of the aneurism wall. The impinged surface is geometry dependent because the blood-stream path flowing in the aneurism is strongly affected by the shape of both the lesion and the diseased arteries. Moreover, the pressure acts on a fragile wall because of the geometry, due to the gap in the media at any branching segment of the cerebral artery network, which has a thinner wall than in extracranial arteries and of the genetics, due to alterations in external and/or internal wall elasticae. A set of factors are neglected: (i) the evolution process because of its long time scale, (ii) the deformability of the lesion and of the vessel because of the much greater stiffness than in other body territories and (iii) the reaction of the living wall, which is unknown. Consequently, the wall is assumed to be passive and the arbitrary aneurism shape corresponds to an intermediate stage of the aneurism evolution; the stress history, characterized by a creep, is already responsible of the large deformation of the artery wall.

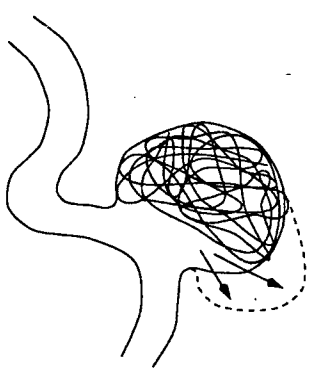

Figure 6: Development of a new aneurismal cavity after intravascular treatment.

2 Method

2.1 Fluid domains

2.1.1 Two-dimensional models

The pathological branching segments of the arterial network, characterized by their geometrical complexity are modeled by planar bifurcations. Two main classes of bifurcations are used to model the congenital cerebral aneurisms: (i) a basillaris-type bifurcation and (ii) an ophtalmica-carotis-type bifurcation.

The geometry of the aneurism neck and of the transition zone affects the local flow and thus the fluid stresses applied on the aneurism wall. However, detailed geometrical data are not available although some lesion sizes can be measured with three-dimensional MR or X-ray angiography. In any cases, the cerebral congenital aneurisms have usually complex configurations. In particular, the neck configuration can not usually be accurately determined. In a first step, two-dimensional models, characterized by a low computation cost, are useful.

Model I may be defined as an aneurism located at an apex of a symmetrical bifurcation of a straight trunk with a transition zone giving birth to two branches. The main geometrical features are: an area ratio of 0.72, a curvature ratio at the bifurcation zone of 0.25, and a circular aneurism (aneurism cavity height to trunk diameter ratio of 2). First numerical simulations were performed on different models of type I, with various neck widths and heights and different implantation zone on the arterial wall (Fig. 7).

Model II is given by a circular aneurism (aneurism height to trunk diameter ratio of 3) developed on the branching segment of a curved arterial segment which gives birth to a small lateral branch. A straight short pipe is used as an entrance segment. The aneurism is located at the apex of an asymmetrical bifurcation of a curved trunk (90 degrees bend, curvature ratio of 1/10). The lateral branch (area ratio of 0.16) is deflected by the aneurism. The short neck is either widely opened on the outer bend (neck diameter to trunk diameter ratio of 0.9 and neck height to trunk diameter ratio of 0.1) or opened on both

the outer trunk wall and the inner branch edge (neck diameter to trunk diameter ratio of 1.6 and neck height to trunk diameter ratio of 0.2) (Fig. 8).

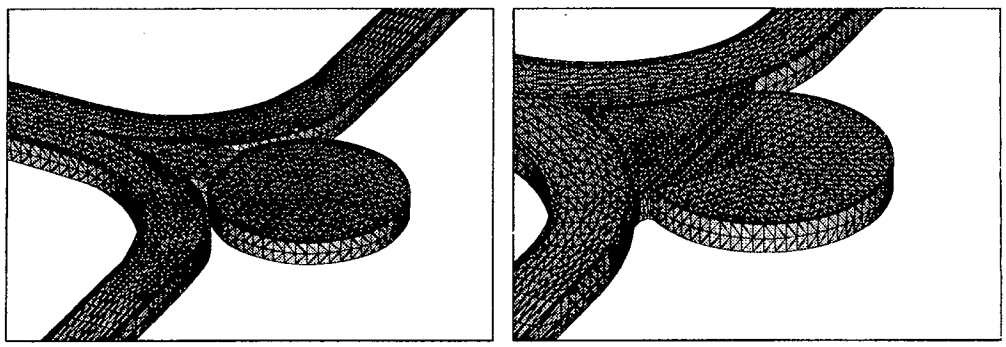

Figure 7: Two-dimensional meshes of intracranial terminal saccular aneurisms (model I). Left: long and narrow neck (neck diameter to trunk diameter ratio of 0.7 and neck height to trunk diameter ratio of 0.25). Right: large neck (neck length to trunk diameter ratio of 1.8).

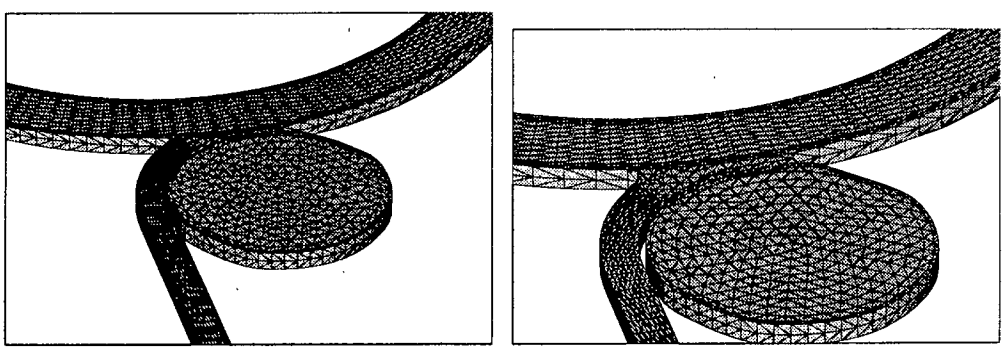

Figure 8: Two-dimensional meshes of intracranial branch saccular aneurisms (model II). Zoom on the transition zone, on the aneurism and the branch entrance region.

But the shape of both models I and II are not sufficiently representative of the shape of usual aneurisms. Consequently, new models have been designed (Fig. 9). The new generation of model I is depicted by the following main geometrical features: same area ratio and curvature ratio of the bifurcation zone as in the first type I models, an apical circular aneurism with a large neck (aneurism radius to trunk radius ratio of 2, neck length to trunk diameter ratio of 1.8). Posttherapeutic aneurisms, completely or partially filled with coils have been modelled; the new cavity wall is either straight or curvilinear according to the most frequently observed configuration (2760 points, 7578 elements) (Fig. 10).

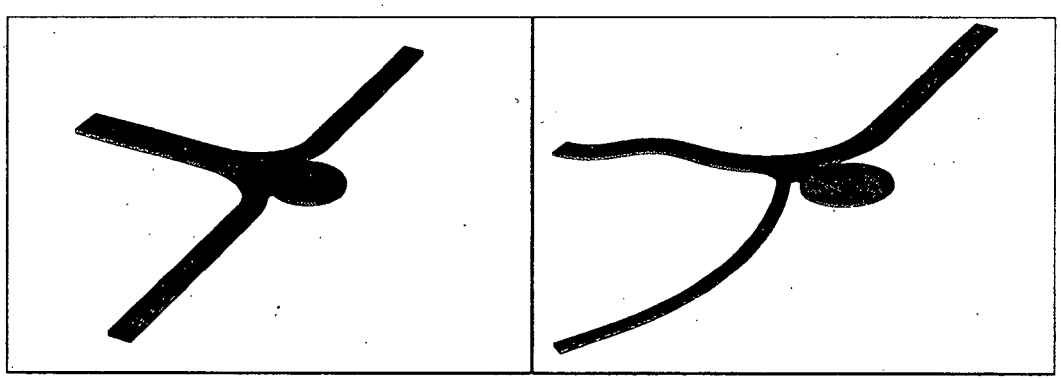

Figure 9: Two-dimensional models of intracranial saccular aneurisms. Model I (left) and model II (right).

Fine mesh is performed in order to explore the influence of the mesh size on the results. The element number ratio is greater than four; fine-mesh model I is composed of 16162 nodes and 46530 elements while coarse mesh model I is made of 3640 vertices and 10128 tetrahedra.

In the new generation of model II, the direction of the curved branch of smaller cross-sectional area (area ratio of 0.25, curvature angle of 75 degrees, curvature ratio of 1/50) is imposed by the surrounding anatomical structures and is not affected by the aneurism (Fig. 9). The elliptical aneurism (aneurism

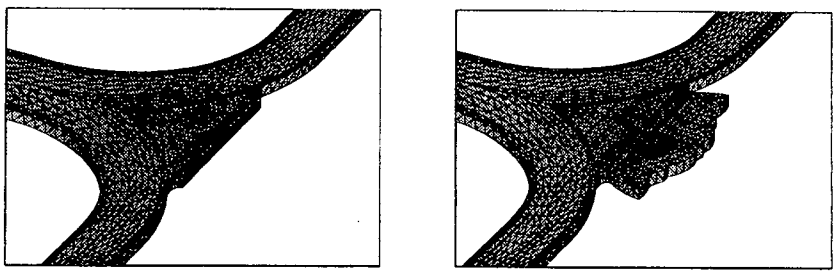

Figure 10: Model I: zooms on an almost completely (left) and partially (right) filled cavity.

ellipticity of 1.2, semi-major axis to trunk diameter ratio of 3.6) is located at the apex of a non-symmetrical branching of a curved trunk (90 degrees bend, curvature ratio of 1/10) downstream from a S-shaped entrance pipe. The short neck is opened on the outer bend and on the entry segment of the inner edge of the branch (neck diameter to trunk diameter ratio of 1.15 and neck height to trunk diameter ratio of 0.2). The pouch is either completely free (4066 vertices, 11118 tetrahedra), completely (3438 vertices, 9327 tetrahedra) or partially filled to mimic the existence of coils (Fig. 11). The shape of the upper wall is assumed to have unsignificant effects on the local flow field. Three configurations are used for demonstration purpose: (i) a very simple one, the straight line (3954 vertices, 10752 tetrahedra), (ii) a curvilinear model of the retracted endoaneurismal new tissues (3942 vertices, 10737 tetrahedra) and (iii) a realistic wavy curvilinear wall (3928 vertices, 10695 tetrahedra).

2.1.2 Three-dimensional models

In a second stage, three-dimensional aneurisms are explored, with the following selection criteria: (i) very good definition of the wall of the region of interest, and (ii) a shape which is typical of one class of aneurisms. The walls of the lesions and the associated artery network are meshed by processing the three-dimensional angiography images (Fig. 12). The region of interest is next determined (Fig. 13). The imaging surface mesh is secondarily converted into a

Figure 11: Aneurism cavity (type II) partially filled with coils with a curvilinear (left), a wavy (mid) and straight (right) upper wall. The wavy border is the more realistic one.

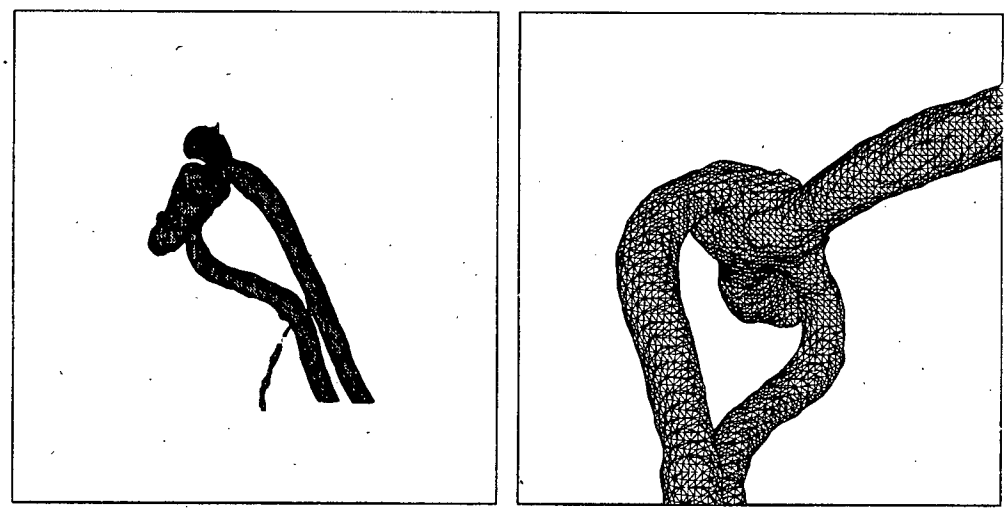

Figure 12: Tri-dimensional mesh of cerebral arteries with an aneurism generated from medical imaging data, obtained by object cuts with planes $x = cst$, $y = cst$, $z = cst$.

surface mesh suitable for fluid flow, associated with a slight surface smoothing and data reduction (Fig. 2.1.2). The arterial explored region is characterized by non-planar curvature and branching.

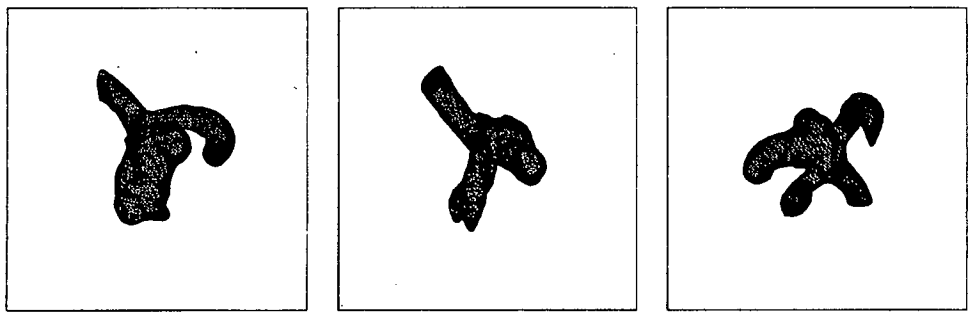

Figure 13: Image processing mesh of the region of interest from X-rays scan data, which is composed of a congenital aneurism with the afferent and efferent arteries from different observation positions.

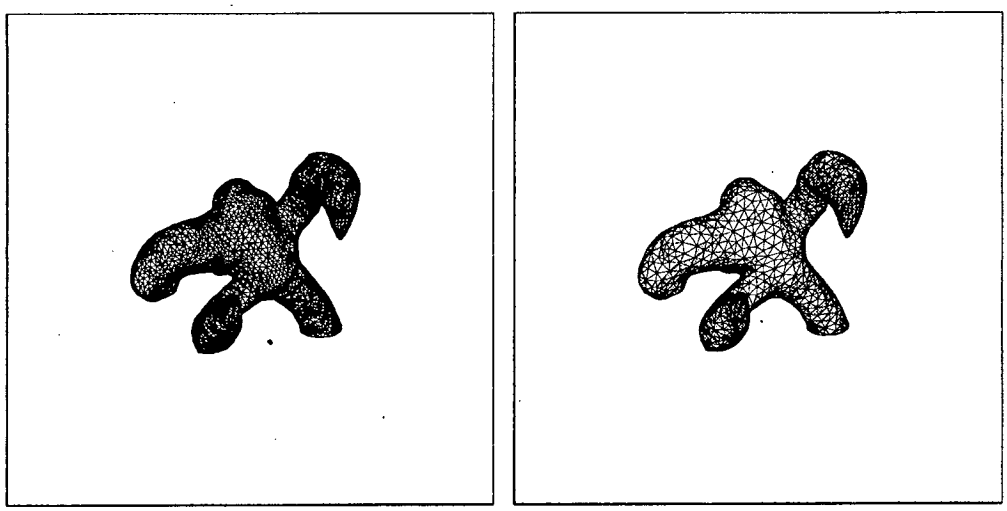

Figure 14: Surface fine (left) and coarse (right) meshes of the region of interest

The three-dimensional mesh of the artery branches ends with exit short straight pipes of length equal to twice the local size of the exit sections. Note that the exit sections do not correspond to vessel cross-sections. The exit-tube axis directions are computed from the mean normal to the normals of the wall element limiting the exit sections. The fluid domain mesh is defined by 8284 nodes and 40168 tetrahedra.

2.2 Numerical simulations

Flow equations The pressure $p(\mathbf{x},t)$ and the fluid velocity $\mathbf{u}(\mathbf{x},t)$ at any point $\mathbf{x}$ of the fluid domain Ω and at5 any time t are computed using the classical fluid mechanics equations,

1. mass conservation:

$$\nabla \cdot \mathbf{u} = 0, \tag{1}$$

2. momentum conservation:

$$\rho\Big(\mathbf{u}_{,t} + (\mathbf{u}\cdot\nabla)\mathbf{u}\Big) = \mathbf{B} - \nabla p + \mu\Delta\mathbf{u}, \tag{2}$$

where ρ and μ are the fluid density and dynamic viscosity.

Let define dimensionless quantities: $\tilde{\mathbf{x}} = \mathbf{x}/L$, $\tilde{t} = tU/L$, $\tilde{\mathbf{u}} = \mathbf{u}/U$, $\tilde{p} = p/(\rho U^2)$, where L and U are the length and velocity scales respectively. The set of equations, without body forces $\mathbf{B}$, become:

$$\tilde{\nabla}\cdot\tilde{\mathbf{u}} = 0, \tag{3}$$

$$\tilde{\mathbf{u}}_{,t} + (\tilde{\mathbf{u}}\cdot\tilde{\nabla})\tilde{\mathbf{u}} = \tilde{\nabla}\tilde{p} + Re^{-1}\tilde{\Delta}\tilde{\mathbf{u}}, \tag{4}$$

where Re is the Reynolds number or the ratio between the inertia forces associated with the convective acceleration ($\rho u\dfrac{\partial u}{\partial x} \propto \rho\, U^2/L$) and the viscous forces ($\mu\dfrac{\partial^2 u}{\partial x^2} \propto \mu\, U/L^2$). In a smooth curved pipe of circular cross section, with small uniform curvature, which conveys a steady laminar motion of incompressible homogeneous Newtonian fluid, the viscous effects can be estimated by the Dean number $De = (R/R_c)^{1/2}Re$, where R/R_c is the ratio between the tube radius R and the curvature radius R_c, the so-called curvature ratio, which is necessary to take into account the centrifugal forces $\propto \rho\, U^2/R_c$.

Flow conditions The fluid was supposed to be incompressible, homogeneous and Newtonian. Steady flow was investigated in the simple two-dimensional models in this preliminary step. A Reynolds number Re, based on the cross-sectional average velocity and the trunk diameter (investigated range: $250 \leq Re \leq 1000$), of 500 corresponds to a fluid (kinematic viscosity of $3\,10^{-6}\ m^2.s^{-1}$) moving with the cross-sectional average velocity at rest of 37.5, 30 or 25 $cm.s^{-1}$ in a vessel of diameter 4 (*i.e.* the cerebral arteries), 5 (*i.e.* the basilar trunk) or 6 mm (*i.e.* the internal carotid arteries). The range of the Dean number De, which is the product of the square root of the stem curvature ratio by the Reynolds number, is $15.6 \leq De \leq 62.5$ and $2.5 \leq De \leq 10$ in model I and II respectively. The wall was assumed to be rigid, because the vessel is confined into an incompressible environment.

Numerical technique The non-linear Navier-Stokes equations are approximated by a discrete representation with physical significance which is aimed at solving a linear system. A weak formulation is obtained from the integral form of the conservation equations, the derivative order of the vector and scalar unknowns of the problem being reduced. The numerical solution technique to solve the classical fluid mechanics equations is the finite element method, suitable to unsteady flow, the time being used as an iterative parameter of the solution.

The basis for the finite element formulation of the set of governing equations is the variational form of the Navier-Stokes equation:

$$\frac{d}{dt}(\mathbf{u},\mathbf{v})+B(\mathbf{u},\mathbf{v})+T(\mathbf{u};\mathbf{u},\mathbf{v})+\ B'(\mathbf{v},p)=<\ l,\mathbf{v}\ >\ ,\ \forall\,\mathbf{v}\in\ V\ \subset\ H^1(\Omega)^3\ , \tag{5}$$

$$B'(\mathbf{u},q)\ =0,\ \forall\,q\in\ Q\ \subset\ L^2(\Omega), \tag{6}$$

where $(\mathbf{u},\mathbf{v})$ is the scalar product associated to the space $L^2(\Omega)$, B and B' are bilinear forms ($B(\mathbf{u},\mathbf{v})\ =\ \frac{1}{Re}\Big[(\nabla\times\mathbf{u},\nabla\times\mathbf{v})_{L^2(\Omega)}+(\nabla\cdot\mathbf{u},\nabla\cdot\mathbf{v})_{L^2(\Omega)}\Big]$ for the set of boundary conditions given in [17], $B'\ =\ -\ (\nabla\cdot\ \mathbf{v},p)$), T is a trilinear form ($T(\mathbf{u};\mathbf{u},\mathbf{v})\ =[(\mathbf{u}\cdot\nabla)\mathbf{u}]\cdot\mathbf{v}$), and $<\ l,\mathbf{v}\ >$ the dual product. The functional space V is defined by:

$$V\ :\ \{\mathbf{v}\in\ H^1(\Omega)^3,\ \mathbf{v}|_{\Gamma_1}\ =0,\ \mathbf{v}|_{\Gamma_2}\ =v_{in}\hat{\mathbf{n}},\ (\mathbf{v}\times\hat{\mathbf{n}})|_{\Gamma_3}\ =0,\ p(\Gamma_3)\ =p|_{\Gamma_3}\ \},$$

$\{\Gamma_i\}_1^3$ being a partition of the boundary Γ of the fluid domain Ω : Γ_1 is the rigid wall on which the classical no-slip condition is applied, Γ_2 and Γ_3 are the flow inlet and outlet sections. The inlet boundary condition is a uniform injection velocity. Constant pressures are set at the outlet section of the straight exit segment of both branches.

The pressure p is defined at the four vertices of the tetrahedron (P_1 element) and the velocity $\mathbf{u}$ at both the vertices and the barycenter (P_1 bubble element). The order of the method is $\mathcal{O}(\xi^2)$ for $\mathbf{u}$ and $\mathcal{O}(\xi)$ for p in the L^2 norm, ξ being the mesh step [18]. The convective term is approximated by the method of characteristics [19]. The computation is initialized as a potential flow. The solution is obtained via a generalized Uzawa-preconditioned-conjugate gradient method [20].

The convergence was supposed to be reached when the L^2 norm of the residuals of the flow quantities are divided at least by a factor 10^{-5}. It is usually obtained at a time lower than the duration of a characteristic path of four tube length, with the suitable time step.

2.3 MR velocimetry

MR examinations were carried out in order to perform in vivo velocimetry (*e.g.* [21][22]). The MR velocimetry was aimed at both giving the boundary conditions and the flow distribution among the branches, which affects the local flow field.

Examinations were performed in 10 normal volunteers and in four patients (male and female in both cases), 30-75 years old, with a 1.5 T scanner (GE Medical Systems). The region of interest of the cerebral artery network was located with a sagittal two-dimensional spin echo sequence (240 mm field of view, 256×192 matrix, slice thickness of 5 mm, 1 excitation). The Willis circle was then imaged with a 3D axial time-of-flight angiography (flip angle of 30 degrees, minimal TE, 240 mm field of view, 256×256 matrix, slice thickness of

0,7 mm, 1 excitation).

Two-dimensional velocity-phase encoded gradient echo sequences (TE of 13 ms, flip angle of 60 degrees, 256×128 matrix, 180 mm field of view, slice thickness of 8 mm, 1 excitation) were gated to the subject's ECG and encoded for a maximum velocity of 2 $m.s^{-1}$, with 4 encoding steps [23].

3 Results

3.1 MR measurements

When the left ventricule ejects blood, part of the energy is transferred to the wall of the large proximal arteries which expand radially [1]. When the systole ends, blood flows backward in the aorta. The retrograde motion induces a rapid fall below the baseline on the velocity wave which is observed as far as the femoral artery. However, the flow remains forward during the whole cardiac cycle in the carotid arteries, although it may decrease to zero during the diastole. Consequently, the blood flow in the cerebral arteries is pulsatile, a time-dependent component being superimposed to a mean flow, such that the flow remains downward in the entire cross section of the cerebral artery throughout the cardiac cycle.

Sectional averages of the blood velocity in the largest cerebral arteries are given in Fig. 15. Due to the set of anastomoses, the flow does not reverse during the cardiac cycle; moreover, the fluid flows with a significant velocity during the low velocity period of the diastolic phase.

MR velocimetry was also aimed at investigating the flow repartition between the branches. Despite the fact that the measurements must be handle with caution, the results show that the blood flow was unevenly distributed in both posterior cerebral arteries in few subjects. Moreover, the ophtalmic artery is too small to be explored, due to the resolution limitation with the MR data acquisition mode used in this study.

[1] The arterial compliance transforms the heart starting-stoping output into a permanent perfusion: this is the so-called "*Windkessel effect*".

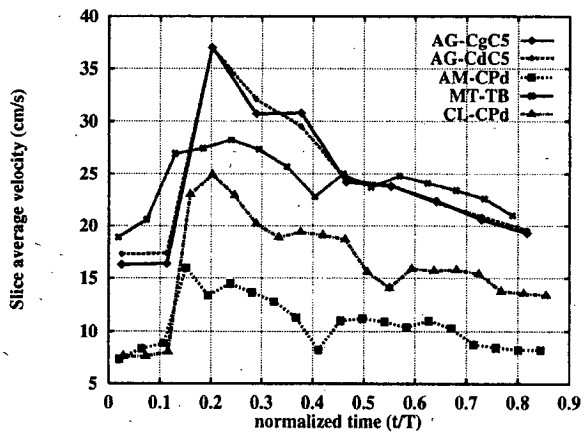

Figure 15: Velocity waveform in the trunks and branches of the Willis circle in healthy volunteers. The blood velocity offset is due to arterial anastomoses. Quantification errors on the velocity component, which is normal to the excited slice, arise mainly from the unknown situation of the cross section of the curved artery and of its small cross-sectional area, which corresponds to the resolution limit of the imaging technique. C5: segment 5 of the internal carotid C artery, CP: posterior cerebral artery, TB: basilar trunk, d: right, g: left)

3.2 Numerical tests

3.2.1 Two-dimensional model I

In the terminal-aneurism model, the liquid coming from the core of the transition zone enters in the central region of the aneurism neck and follows a curved path within the aneurismal sac to exit along the side walls and the lips into the corresponding branches (Fig. 16). The velocity magnitude decreases from the neck to the dome. The velocity along the fundus wall is small, but the fluid does not stagnate. The rotatory streams in the cavity are either symmetrical or asymmetrical (Fig. 17). When the flow distribution is asymmetrical, the dominant side stream enters in the fundus and skirts the dome wall, while the dominated one is bounded by the dominant stream and the corresponding side wall. A single swirl expands from the left edge of the transition zone, towards the neck, around which the fluid rotates. In numerical tests with strong non-uniform flow distribution, the fluid from one half of the transition zone is conveyed directly to the corresponding branch while the aneurism cavity is irrigated by the fluid coming from the second transition zone side; the boundary between the influxes reaches the aneurism lip, where the pressure is high. The outflow moves then exclusively into one branch.

The pressure field inside the aneurism sac, which faces the straight trunk, reaches its highest values within the whole cavity. The dome is susceptible to break. When the fluid flows unevenly among the branches, a space pressure gradient occurs between the lateral walls of the cavity. The location of the highest pressure zone within the cavity moves away from the neck when Re decreases.

Flow separation regions appear at the bifurcation outer edge (inner wall with respect to the center of curvature) of the transition zone. When the between-branch flow is not equal, another flow separation region occurs at the inner bifurcation wall in the entrance segment of the branch which conveys the main part of the aneurism outflow. The transition zone flow separation in the same side spreads out, while the flow separation in the opposite side disappears. The stronger the inertial effects, the greater the recirculation zones.

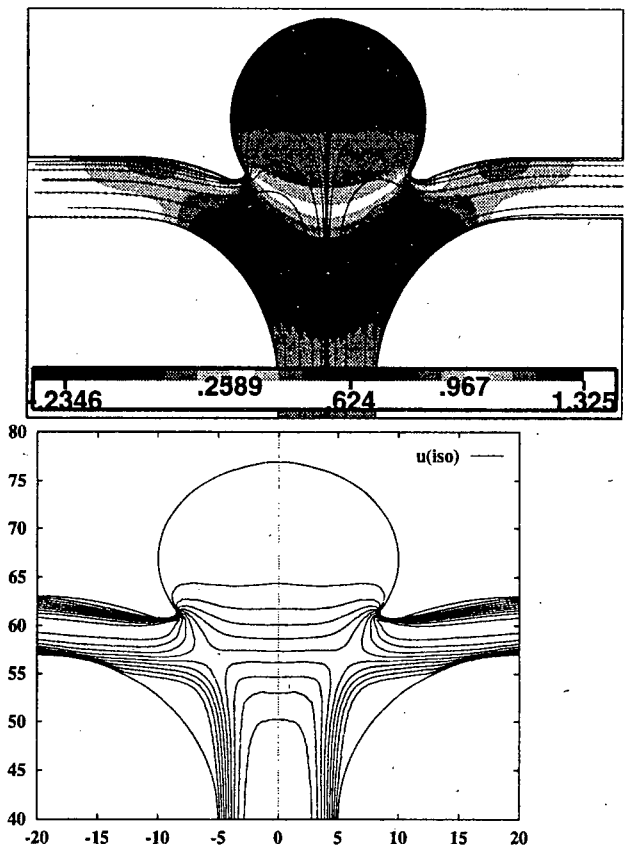

Figure 16: Streamlines, pressure field (left) and velocity isocountours (right) in model I. Both symmetrical geometry and flow; laminar flow ($Re = 500$).

When the aneurism is obliterated, the fluid is conveyed along the new obliteration wall into both branches. Flow separation regions at the outer edge of the transition zone have nearly the same area than before treatment. The pressure reaches its highest values at the central part of the new wall, like it does with a normal bifurcation apex [17]. The bulk flow features do not depend on the Reynolds number.

The liquid circulation in a partially filled cavity ressembles to the flow in an untreated aneurism, except that the large low flow region within the pouch disappears. A large high-pressure region is located at the fundus center and two small high-pressure regions are observed at both edges. When the flow distribution is uneven, the pressure is higher on the aneurism wall which faces the inflow orifice zone, while the fluid flows between the posttherapeutic wall and the lateral transition zone vortex.

3.2.2 Two-dimensional model II

In the branch-aneurism model, a swirl occurs in the neck and the transition zone, the fluid flowing from the downstream lip of the neck, where the aneurism velocity is the highest, to the upstream one, which leads to the branch wall (Fig. 18 and 19). The inflow and outflow regions are the distal and proximal lip respectively. The fluid swirls in the entry portion of the aneurismal sac. A second low-speed vortex, induced by viscous effects, holds the major part of the cavity, without convecting the fluid along the dome wall at mid-range Reynolds number. A flow separation region appears at the bifurcation inner wall in the entrance segment of the branch, near the aneurism lip.

The pressure reaches its maximal values at the outer stem wall very close to the dowstream lip. It is greater in the cavity than in the main part of the transition-zone lumen, The highest pressure region in the sac is observed near the aneurismal edge close to the upstream lip, whereas the lowest pressure region is located near the aneurism center.

When the aneurism is completely blocked, the transition zone vortex is bounded by the stream flowing along the outer bend wall. The pressure is

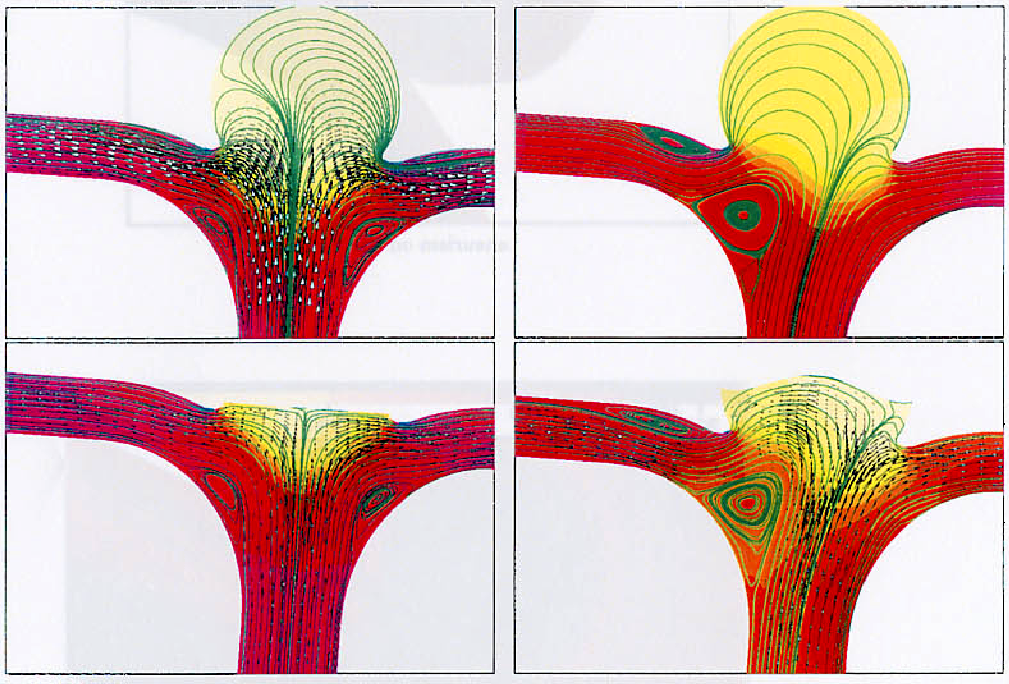

Figure 17: Streamlines and pressure field (grey code: black for minimum, white for maximum) in model I. Top: untreated aneurism (left: Re = 1000, flow ratio between the left branch and the right branch $Q_{lb}/Q_{rb} = 0.97$, right: Re = 500, $Q_{lb}/Q_{rb} = 1.5$). Bottom: almost completely (left panel, $Q_{lb}/Q_{rb} = 1.0$) and partially (right panel, $Q_{lb}/Q_{rb} = 1.2$) filled cavity (Re = 500).

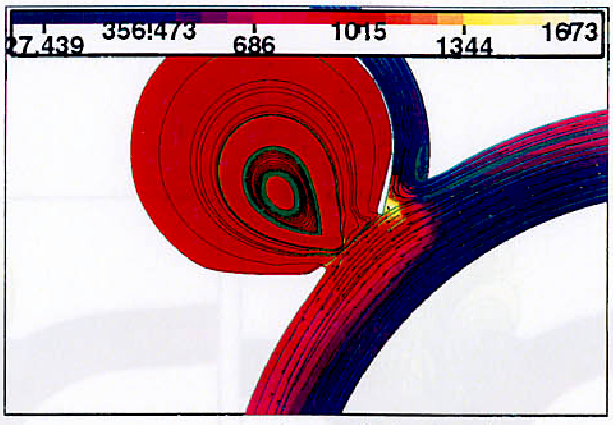

aneurism on the trunk wall

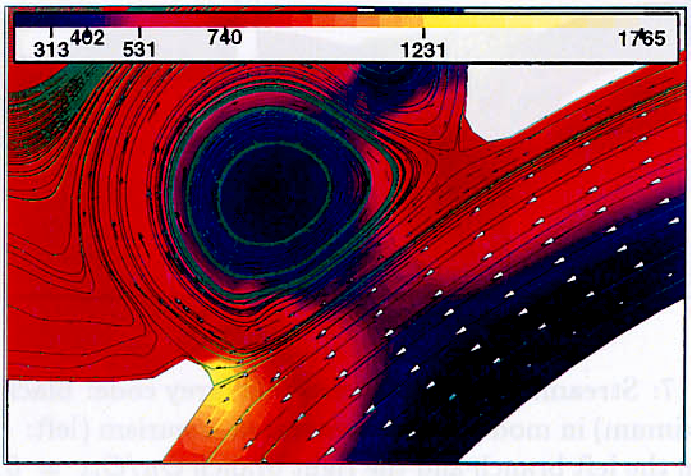

aneurism on the trunk and branch walls

Figure 18: Velocity vectors, streamlines and pressure field in two-dimensional aneurism model II. Laminar flow ($Re = 500$).

maximum at the downstream lip. In a partially filled cavity, the results do not depend on the wall shape; it is useless to mimic the reality, especially when two-dimensional models are used. The pressure, which remains the highest at the dowstream lip, is greater in the fundus region which is close to the branch than the part close to the trunk. A high pressure zone occurs at the boundary between the upstream lip and the adjoining lateral wall.

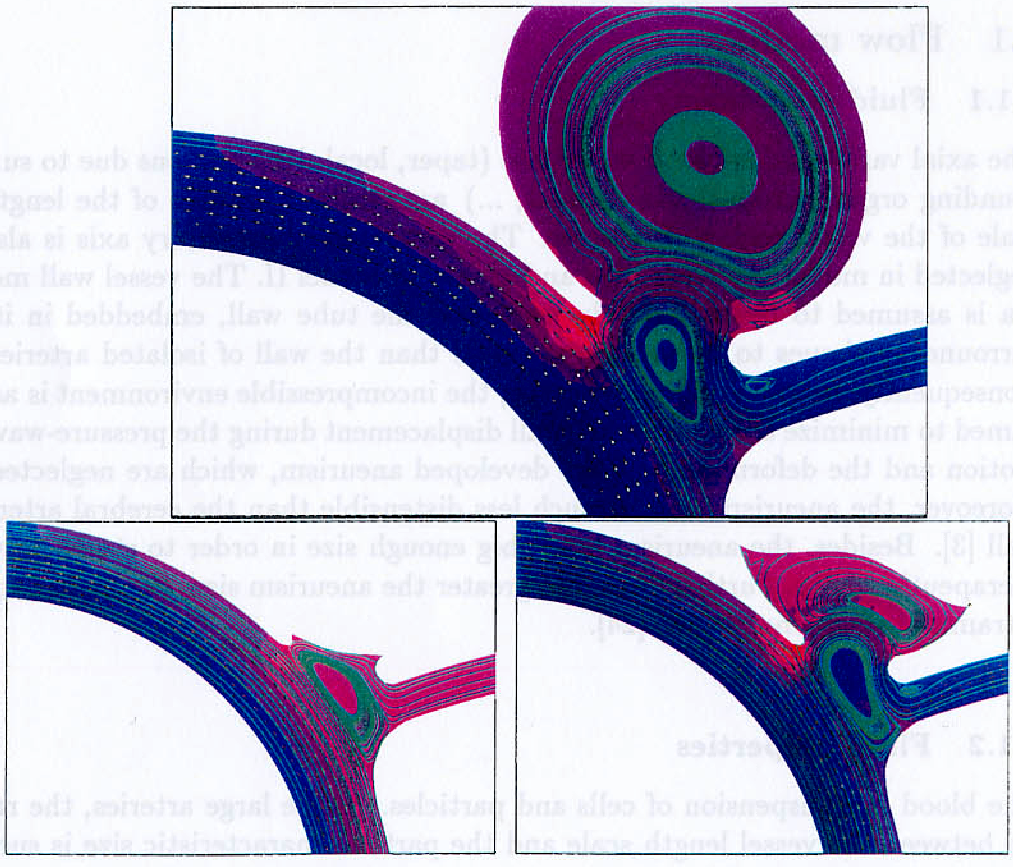

Figure 19: Streamlines and pressure field in model II. Top: untreated aneurism, bottom: almost completely (left) and partially (right) filled cavity (Re = 500).

3.2.3 Three-dimensional model

Velocity isocontours and streamlines are displayed in Fig. 3.2.3, 3.2.3 and 3.2.3. The bulk flow properties are similar to the two-dimensional model results, defined by aneurism swirls, low dome flow and high pressure zones.

4 Discussion

4.1 Flow models

4.1.1 Fluid domains

The axial variations in blood vessel size (taper, local deformations due to surrounding organs, cross-shape changes, ...) are omitted because of the length scale of the vessel region of interest. The curvature of the artery axis is also neglected in model I or simplified and planar in model II. The vessel wall media is assumed to be in a steady state and the tube wall, embedded in its surrounding tissues to be much more rigid than the wall of isolated arteries. Consequently, in this preliminary stage, the incompressible environment is assumed to minimize both the vessel-wall displacement during the pressure-wave motion and the deformation of the developed aneurism, which are neglected. Moreover, the aneurism wall is much less distensible than the cerebral artery wall [3]. Besides, the aneurism has a big enough size in order to study post-therapeutic cavity. Furthermore, the greater the aneurism size, the higher the intramural stress magnitude [24].

4.1.2 Fluid properties

The blood is a suspension of cells and particles. In the large arteries, the ratio between the vessel length scale and the particle characteristic size is such that the blood is considered as a continuous homogeneous medium. The red blood cells RBC play a major role on the rheological behaviour of the blood due to both their size and number. The blood has, in steady state conditions, a shear-thinning behaviour [26]. The sigmoïd relationship between the shear rate $\dot{\gamma}$ and the fluid viscosity μ is explained by RBC agregation at low shear

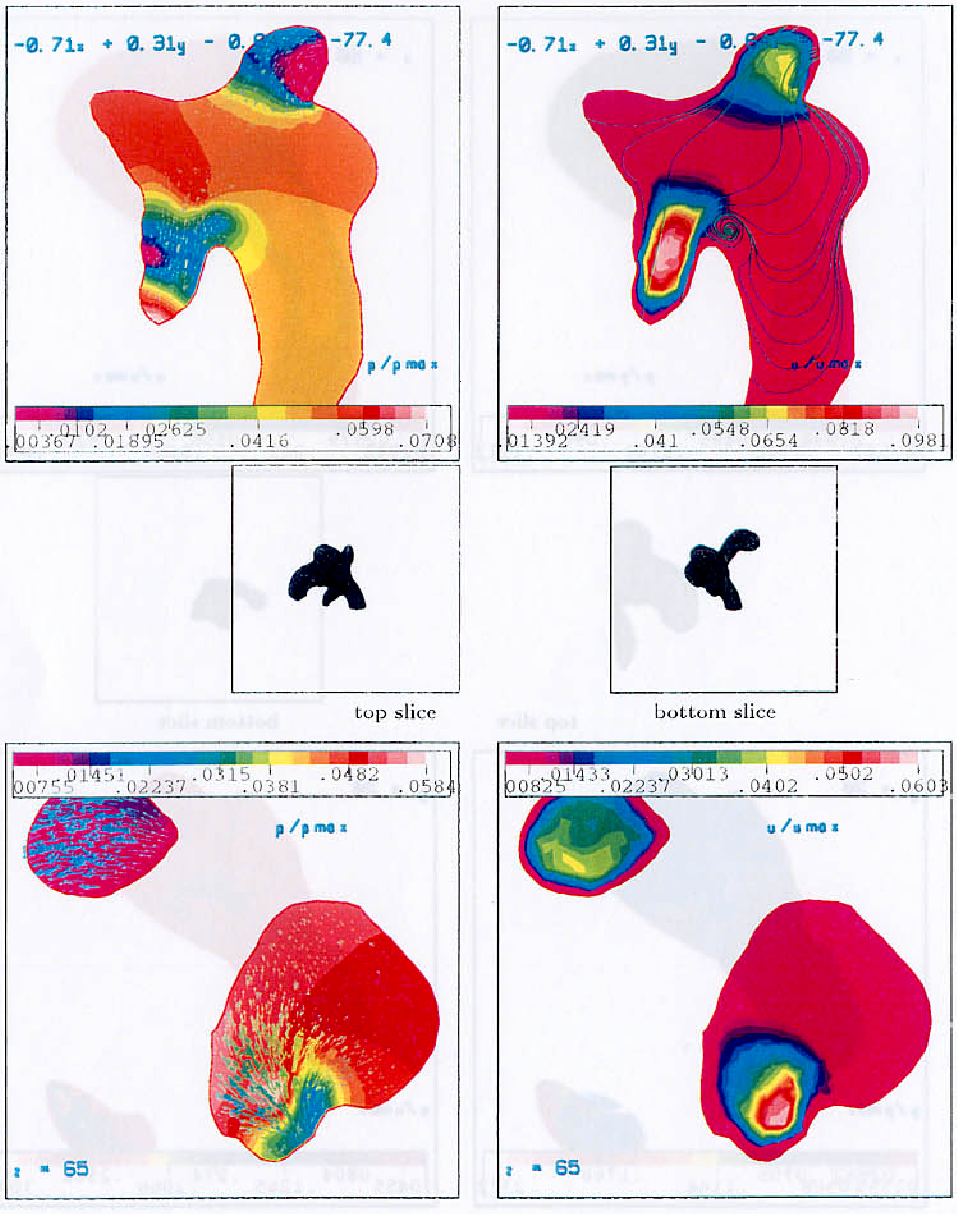

Figure 20: Pressure field with velocity vectors (left) and velocity isocontours (right) in arbitrary given planes (see joint figures, second row, left panel for the top displayed slice and right panel for the bottom displayed slice) of a tri-dimensional cerebral aneurism. Laminar flow ($Re = 500$).

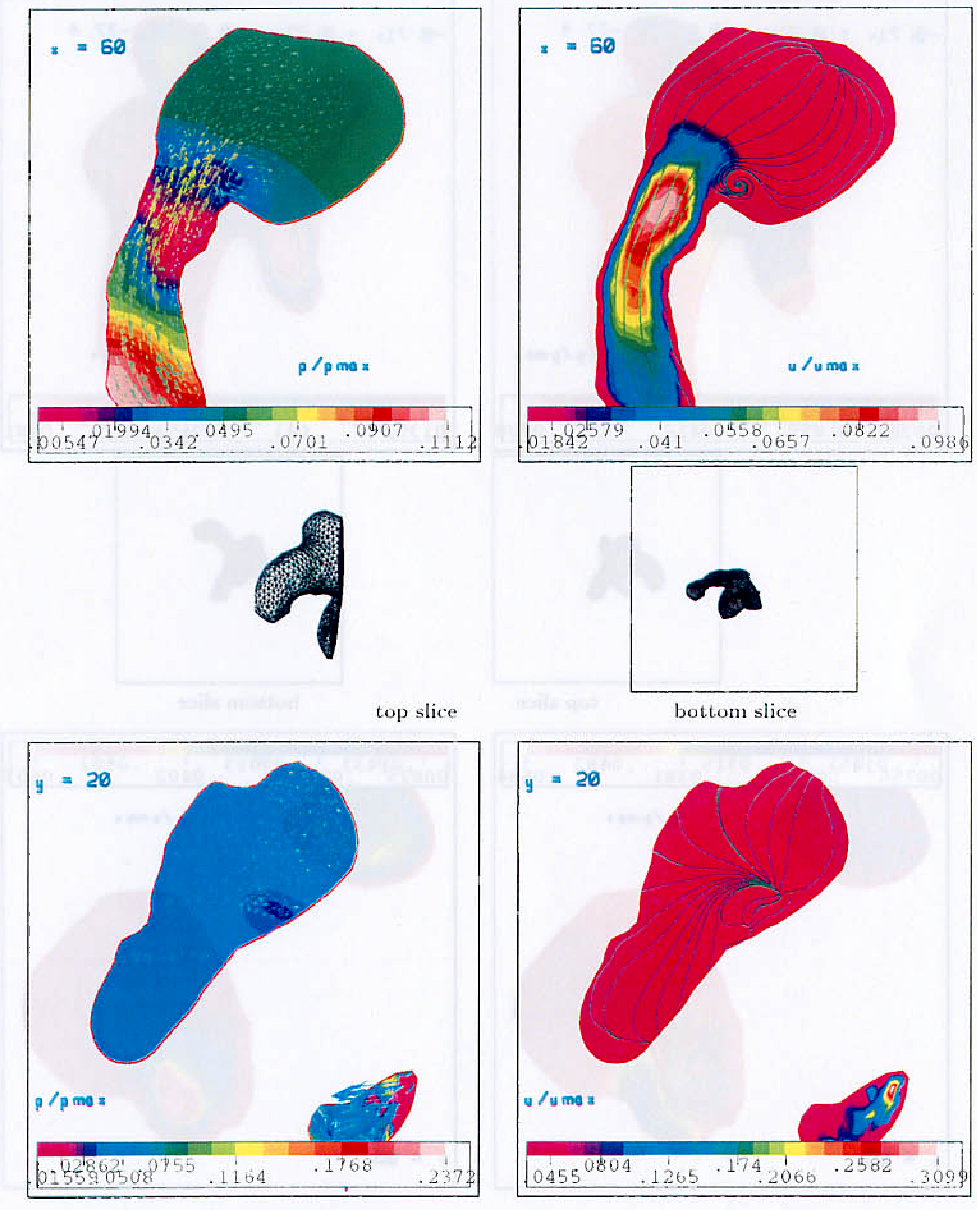

Figure 21: Pressure field with velocity vectors (left) and velocity isocontours with streamlines (right) in arbitrary given planes (see joint figures, second row, left panel for the top displayed slice and right panel for the bottom displayed slice) of a tri-dimensional cerebral aneurism. Laminar flow ($Re = 500$).

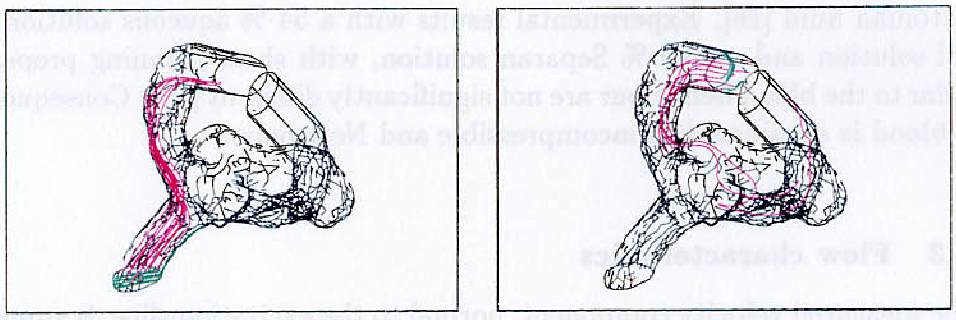

Figure 22: Streamlines originated from a station near the trunk entrance (left) and from the aneurism cavity near the neck (right).

rates associated to high viscosity values in the one hand while RBC deformation and orientation lead to a low viscosity plateau μ_∞ at high shear rates $\dot{\gamma} \geq \sim 10^2\, s^{-1}$ (Newtonian behaviour). There is a huge between-subject variability of the μ *vs.* $\dot{\gamma}$ relationship. The viscosity maximum μ_0, which is difficult to measure with available experimental devices, is about 10 times greater than μ_∞ in steady states. When both RBC agregation and deformation are inhibited, μ_0 is close to μ_∞ [27].

In large arteries, the red blood cells, expelled from the heart cavities where they have been shaked, are expected neither to deform nor to agregate owing to a short convection time scale with respect to the characteristic agregation time. However, in the low flow region of the aneurism cavity along the dome wall where the residence time of particles and conveying cells is much greater, the red blood cell agregation time can be supposed to have the same order of magnitude than the local flow time scale. Non-Newtonian fluid flow must then be simulated. However, the generalized Newtonian model used to mimic the shear-thinning blood behaviour, mainly due to red blood cell agregation and deformability, gets its input data from experimental results obtained in steady state conditions, far from the physiological ones (*e.g.* [28]). Furthermore, numerical tests in a two-dimensional symmetric bifurcation with a non-symmetric aneurism show minor differences in velocity field between non-Newtonian and

Newtonian fluid [16]. Experimental results with a 54 % aqueous solution glycerol solution and a 0.04 % Separan solution, with shear-thinning properties similar to the blood behaviour are not significantly different [15]. Consequently, the blood is considered as incompressible and Newtonian.

4.1.3 Flow characteristics

If the measured velocity component, normal to the excitation slice, is supposed to be the main velocity component, several assumptions must be made: (i) the vessel exploring slice is approximately the actual cross section, (ii) the cross currents are negligible, (iii) the direction of the measured component remains constant through the slice thickness. The whole set of hypotheses can not be satisfied; qualitative data can only be obtained. Furthermore, the MR velocimetry only estimates the slice average velocity because the artery transverse area is too small to avoid quantification errors. Further studies must thus be carried out to get the input conditions.

Flow feature changes between steady and one-harmonic pulsatile flows can be as large as between non-zero mean oscillatory and suitable physiological flows, characterized by strong time gradients during the acceleration phase (*e.g.* [29]). Besides, there is no experimental evidence that flow one-harmonic pulsatility affects significantly the aneurism velocity field [15]. Steady flows are hence studied in the present work, which is mainly dealing with mechanical risk factors, before and after endovascular treatment, rather than with a detailed quantification of the flow field.

4.1.4 Meshes and finite element approximations

The influence of the mesh size on the results is studied on the untreated model I. The element number ratio is greater than four; model I is either composed of 16162 nodes and 46530 elements, or 3640 vertices and 10128 tetrahedra. The dimensions of the swirls and flow recirculations depends on the mesh size; they are larger when the element number is lower. However, the bulk flow

properties remains unchanged.

Finally, because unique solution of the Navier-Stokes equations has not been demonstrated, another finite element technique has been used [30]. The incompressible Navier-Stokes solver is based on Chorin's projection method. The computation of intermediate velocity is done explicitely and the stabilization of convection terms is based on positive streamwise invariant residual distribution scheme. The Poisson problem for pressure is solved using conjugate gradient technique. Again, the flow behaviour is similar for given flow conditions and boundary conditions.

4.2 Literature data

The following flow features are usually observed in aneurism region of the arterial network: (i) a swirl in the fundus of the cavity, the fluid flowing from the downstream lip of the neck, where the aneurism velocity is the highest, to the upstream one, whereas the velocity in the dome is very low, (ii) flow separation at the outer bifurcation wall in front of the aneurism and further downstream at the inner wall of the entrance segment of both branches in the model of lateral aneurism, developed on the apex and on a single branch, in a symmetrical bifurcation [16] and, at higher Reynolds number, a second swirl in the core region of the carrying branch. Our results are in agreement with these data.

Asymmetrical flow in symmetrical terminal aneurisms is observed between both sides of the aneurismal sac. Stream visualization, at $Re = 500$, in rigid models (area ratio of 1.02, bifurcation angle of 135 degrees) with uni- (neck and sac diameter of 0.7 and 2.9 d respectively) and bilocular (neck and sac diameter of 0.7 and 3.3 d respectively) terminal aneurisms shows that the trunk axial stream is deflected laterally in the pouch and goes mainly in one branch, adjoining to the major outflow neck zone [14]. However, this flow features can be due to uncontrolled asymmetries of the test section and/or in the experimental bench. But experimental evidence of asymmetrical flow in planar symmetrical domain (area ratio of 0.98, bifurcation angle of 140 degrees, neck width of 1 d, sac diameter of 1.4 d, orifice-to-dome length of 1.5 d) is

provided when the branch flow rates are equal, either in steady conditions or in non-zero mean sinusoidal flow ($\overline{\text{Re}}$ of 500, St of 6.7) [15]. Besides, the velocity magnitude at the neck center is 3.3 to 8 times greater than the one at the fundus center. The flow asymmetry rises when the flow ratio between the branches is 1/3. The same investigators did not observed such flow asymmetry within the pathological region in angled terminal aneurism (angle between the stem axis and the sac axis of 45 degrees). These authors concluded that the fluid domain geometry is the main factor which affects the aneurismal flow much more than the wall deformability, the flow pulsatility anf the fluid properties.

5 CONCLUSION

The two-dimensional models, characterized by a well defined geometry and low computational cost, give promising results, in particular high pressure zones susceptible to be sources of futur development of the wall dilatation and rupture. The rupture risk and failure of endovascular treatment is associated, at least partially, to the aneurism geometry. The neck swirl, the dome slow flow and the branch flow separation define the set of aneurism flow properties, which are observed in a three-dimensional aneurism, the shape of which is obtained by medical imaging. Two-dimensional models are then useful to understand the bulk aneurism flow.

The set of results may be validated by the experimental data obtained either on animal models, modelling the same configuration (which do not represent the pathology here investigated), or on physical models of the explored three-dimensional aneurism, using the laser cut-out technique to obtain the same lesion-wall surface. In the future, computations can be performed with boundary conditions obtained from technically improved magnetic resonance or ultra-sound velocimetry. But, because of the huge variability of the lesions, the artery-like model study may be also aimed at defining some good aneurism models.

References

[1] Austin G., Equation for model intracranial aneurysm with consideration of small dissipation term. Math. Biosci., **22** (1974), 277-291.

[2] Cronin J., Mathematical model of aneurysm of the circle of Willis: II: a qualitative analysis of the equation of Austin. Math. Biosci., **22** (1974), 237-275.

[3] Ferguson G.G., Physical factors in the initiation, growth and rupture of human intracranial saccular aneurysms. J. Neurosurg., **37** (1972), 666-677.

[4] Budwig R., Elger D., Hooper H. and Slippy J., Steady flow in abdominal aortic aneurysm models. ASME J. Biomechanical Engineering, **115** (1993), 418-423.

[5] Bluestein D., Niu L., Schoephoerster R.T. and Dewanjee M.K., Steady flow in an aneurysm model: Correlation between fluid dynamics and blood platelet deposition. ASME J. Biomechanical Engineering, **118** (1996), 280-286.

[6] Turjman F., Massoud T.F., Sayre J. and Vinuela F. Predictors of aneurysmal occlusion in the period immediately after endovascular treatment with detachable coils: a multivaraite analysis. AJNR Am. J. NeuroRadiol., **19** (1998), 1645-1651.

[7] Liepsch D.W., Stieger H.J., Poll A. and Reulen H.J., Hemodynamic stress in lateral aneurysms Biorheology, **24** (1987), 689-710.

[8] Aenis M., Stancampiano A.P., Wakhloo A.K. and Lieber B.B., Modeling of flow in a straight stented and nonstented side wall aneurysm model. ASME J. Biomechanical Engineering, **119** (1997), 206-212.

[9] Low M., Perktold K. and Raunig R. Hemodynamics in rigid and distensible saccular aneurysms: a numerical study of pulsatile flow characteristics. Biorheology, **30** (1993), 287-298.

[10] Niimi H., Kawano Y. and Sugiyama I., Structure of blood flow through a curved vessel with an aneurysm Biorheology, **21** (1984), 603-615.

[11] Graves V.B., Strother C.M., Partington C.R. and Rappe A., Flow dynamics of lateral carotid artery aneurysm and their effects on coils and ballons: an experimental study in dogs AJNR Am. J. NeuroRadiol., **13** (1992), 189-196.

[12] Strother C.M., Graves V.B. and Rappe A., Aneurysm hemodynamics: an experimental study AJNR Am. J. NeuroRadiol., **13** (1992), 1089-1095.

[13] Kerber C.W., Heilman C.B. and Zanetti P.H., Transparent elastic arterial models I: a brief technical note. Biorheology, **26** (1989), 1041-1049.

[14] Roach M.R., Scott S. and Ferguson G.G. The hemodynamic importance of the geometry of bifurcations in the circle of Willis Stroke, **3** (1972), 255-267.

[15] Steiger H.J., Liepsch D.W., Poll A. and Reulen H.J. Hemodynamic stress in terminal saccular aneurysms: a laser-Doppler study. Heart Vessels, **4** (1988), 162-169.

[16] Perktold K., Peter R. and Resch M., Pulsatile non-newtonian blood flow simulation through a bifurcation with an aneurysm. Biorheology, **26** (1989), 1011-1030.

[17] Conca C., Pares C., Pironneau O., Thiriet M., A computational model of Navier-Stokes equations with imposed pressure and velocity fluxes. Int. J. Numer. Methods in Fluids, **20** (1995), 267-287.

[18] Arnold D.N., Brezzi F. and Fortin M., A stable finite element for the Stokes equations. Calcolo, **21** (1984), 337-344.

[19] Pironneau O., On the transport-diffusion algorithm and its application to the Navier-Stokes equations. Numerische Mathematik, **38** (1982), 309-332.

[20] Glowinski R., *Numerical methods for nonlinear variational problems* Springer Series in Computational Physics, (Springer-Verlag, New York, 1984).

[21] Idy-Peretti I., Bittoun J., Bases Physiques de l'IRMN, in *IRMN corps entier*, edited by D. Vanel (Springer-Verlag, 1988).

[22] Thiriet M. et al., Apports et limitations de la vélocimétrie par résonance magnétique nucléaire en biomécanique. Mesures dans un embranchement plan symétrique. J. Phys. III France, **7** (1997), 771-787.

[23] Bittoun J. et al., High-precision MR velocity mapping by 3D-Fourier phase encoding with small number of encoding steps, Magn. Reson. Med., **29** (1993), 674-680.

[24] Kyriacou S.K. and Humphrey J.D., Influence of size, shape and Properties on the mechanics of axisymmetric saccular aneurysm. J. Biomechanics, **29** (1996), 1015-1022.

[25] Thiriet M. et al., Computational models of flow in cerebral aneurisms. J. Biomechanics, **31**, spt. 1 (1998), 20.

[26] Chien S., Shear dependence of effective cell volume as a determinant of blood viscosity, Science, **168** (1970), 977-978.

[27] Chien S., Biophysical behavior in suspensions, in *The Red Blod Cell*, edited by D. Surgenor (Academic Press, New York, 1975).

[28] Thiriet M., Martin-Borret G., Hecht F., Ecoulement rhéofluidifiant dans un coude et une bifurcation plane symétrique. Application à l'écoulement sanguin dans la grande circulation. J. Phys. III France, **6** (1996), 529-542.

[29] Siouffi M., Pelissier R., Farahifar D., Rieu R., The effect of unsteadiness on the flow through stenoses and bifurcations. J. Biomechanics, **17** (1984), 299-315.

[30] Medić G. and Mohammadi B., NSIKE - an incompressible Navier-Stokes solver for unstructured meshes Rapport de Recherche INRIA no. 3644, 1999.

Contents

Unité de recherche INRIA Rocquencourt
Domaine de Voluceau - Rocquencourt - B.P. 105 - 78153 Le Chesnay Cedex (France)

Unité de recherche INRIA Lorraine : Technopôle de Nancy-Brabois - Campus scientifique
615, rue du Jardin Botanique - B.P. 101 - 54602 Villers lès Nancy Cedex (France)
Unité de recherche INRIA Rennes : IRISA, Campus universitaire de Beaulieu - 35042 Rennes Cedex (France)
Unité de recherche INRIA Rhône-Alpes : 655, avenue de l'Europe - 38330 Montbonnot St Martin (France)
Unité de recherche INRIA Sophia Antipolis : 2004, route des Lucioles - B.P. 93 - 06902 Sophia Antipolis Cedex (France)

Éditeur
INRIA - Domaine de Voluceau - Rocquencourt, B.P. 105 - 78153 Le Chesnay Cedex (France)
http://www.inria.fr
ISSN 0249-6399